Available online at www.sciencedirect.com

ScienceDirect

Ceramics International 39 (2013) 9637–9644

CERAMICS INTERNATIONAL

www.elsevier.com/locate/ceramint

Effect of Al^{3+} on the growth of ZnO nanograss film and its application in dye-sensitized solar cells

Shibu Zhu[a], Xin Tian[a], Liming Shan[a], Zhaoying Ding[a], Zhengxing Kan[a], Xiaoling Xu[a], Zuowan Zhou[a,*], Li Wang[b]

[a]*Key Laboratory of Advanced Technologies of Materials (Ministry of Education), School of Materials Science and Engineering, Southwest Jiaotong University, Chengdu 610031, PR China*

[b]*China Academy of Space Technology, Beijing 100094, PR China*

Received 11 April 2013; received in revised form 21 May 2013; accepted 21 May 2013
Available online 28 May 2013

Abstract

ZnO nanorod arrays were synthesized by an aqueous solution process with Al^{3+} as an adjusting agent, and their performances as photoanodes of dye-sensitized solar cells (DSSC) were investigated. The ZnO nanorods were characterized by scanning electron microscopy (SEM) and X-ray photoelectron spectroscopy (XPS). It was found that adding Al^{3+} during the growth procedure not only changed the morphology and aspect ratio but also affected the chemical features of the ZnO nanorods. The ZnO nanograss films were evaluated as photoanodes for DSSC. The photovoltaic results showed that the overall conversion efficiency of DSSC based on ZnO nanorods obtained from the growth solution containing 2 at% Al^{3+} was increased by 55.6% as compared to that without Al^{3+}. This significant improvement was attributed to the reduced charge recombination and enhancement of the electron lifetime.

Keywords: ZnO nanograss; Aluminum ion; Solution method; Dye-sensitized solar cell

1. Introduction

Since porous nanocrystalline titanium dioxide (TiO_2) were used as electrode materials, and a conversion efficiency of 7.1% was obtained by Grätzel et al. in 1991, dye-sensitized solar cells (DSSC) are regarded as the promising photovoltaic devices in the decades due to their low cost and high efficiency of photo to electric conversion and eco-friendly production [1,2]. Nowadays, the highest conversion efficiency of DSSC based on porous TiO_2 film has exceeded 12% [3]. Besides TiO_2, other n-type binary metal oxide semiconductors can be used in DSSC in principle, such as ZnO, Fe_2O_3, SnO_2, Nb_2O_5 and so on [4]. Among these materials, ZnO has attracted more attentions since it possesses a similar band-gap structure but a higher electronic mobility compared to TiO_2 [5]. What is more, it is easier to obtain highly crystallized ZnO and various morphologies [6–8]. In the past decades, DSSC based on ZnO nanostructures have been reported by many groups [9–13]. ZnO 1-D nanostructures, such as nanotubes [14,15] and nanowires [16,17] have been extensively studied. The purpose for using ZnO 1-D nanostructures is expected to significantly enhance the electron transport efficiency in the photoelectrode films by providing a direct conduction pathway for the rapid collection of photogenerated electrons, therefore reducing the number of interparticle hops.

Although the results obtained from 1-D ZnO nanostructures have shown relatively lower conversion efficiency than those from TiO_2, it is still regarded as a promising alternative to TiO_2 due to its superior properties. However, the insufficient surface area of 1-D ZnO nanostructures seems to be the primary factor that limits the amount of dye adsorption as well as the conversion efficiency of the cells. One of the effective approaches to solve this problem is to reduce the diameter of the nanowires/nanorods, thus increasing the density of the array [18,19]. Many groups had reported that the aspect ratio of ZnO nanorods/wires could be controlled by adding polymer capping agent, such as poly(ethylenimine) (PEI). For example,

*Corresponding author. Tel./fax: +86 28 87600454.
E-mail address: zwzhou@at-c.net (Z. Zhou).

0272-8842/$ - see front matter © 2013 Elsevier Ltd and Techna Group S.r.l. All rights reserved.
http://dx.doi.org/10.1016/j.ceramint.2013.05.085

Law et al. [10] reported that the introduction of PEI into the growth solution as an additive could efficiently increase the length of ZnO nanowire arrays, receiving ZnO nanowires with an aspect ratio above 125, which is the enlarged inter surface area for dye loading in DSSC application. Recently, Joo et al. [20] found that the geometry of hydrothermally grown ZnO nanowires can be tuned from platelets to needles by introducing ancillary non-zinc sulfates, covering more than three orders of magnitude in aspect ratio (~0.1–100). To our best knowledge, there has been no thorough report on the electrochemical details of ZnO nanograss, prepared by hydrothermal methods modified by metal ion, used as photoanode materials in DSSC.

Thus, in the present work, we preliminarily synthesized ZnO nanograss *via* the aqueous solution method by introducing Al^{3+} as an additive. The effect of Al^{3+} concentration varying from 0 to 1 mM on the structure and micro-morphology of ZnO nanograss films grown on FTO substrates was examined. In this case, the Al^{3+} not only affected the aspect ratio of ZnO nanograss, but also affected the oxygen defect in the skin layer of ZnO. The photovoltaic conversion properties in dye-sensitized solar cells (DSSC) were also discussed.

2. Experimental

2.1. Synthesis of ZnO nanograss

All chemicals in this experiment were of analytical grade and used as received. Fluorinated tin oxide (FTO, 15 Ω cm^{-2}, Nippon Sheet Glass, Japan) were rinsed ultrasonically in acetone, ethanol and distilled water for 15 min, respectively. Synthesis of zinc oxide (ZnO) nanograss was similar to our previous report with a small difference [18]. A typical procedure as follows: a ZnO seed layer was prepared on FTO glass by dip-coating (3 cm/min) in 5 mM ethanolic solutions of zinc acetate, followed by thermal decomposition at 300 °C for 15 min. The obtained seed layer covered FTO glasses were then transferred into a growth solutions of 25 mM zinc nitrate ($Zn(NO_3)_2 \cdot 6H_2O$, Aladdin), 25 mM hexamethylenetetramine (HMTA, Aladdin) and different concentrations (0, 0.25, 0.5 and 1 mM) of aluminum nitrate ($Al(NO_3)_3 \cdot 9H_2O$, Chengdu Kelong chemical), and hydrothermal reaction was carried out at 92 °C for 20 h. The growth solutions were refreshed every 4 h during the reaction period. Then the FTO glasses covered by ZnO films were taken out to rinse with deionized water and dried at room temperature. The obtained samples were named as Al-0, Al-0.25, Al-0.5 and Al-1, respectively.

2.2. Fabrication of DSSC

The as-prepared ZnO nanograss films were sensitized into 0.3 mM solution of $(Bu_4N)_2Ru(dcbpyH)_2(NCS)_2$ (N719 dye, Dyesol, Australia) in dry ethanol for 3 h, followed by cleaning with absolute ethanol to remove redundant dye. A chemically platinized FTO counter electrode was placed over the dye-sensitized electrode, and then the electrolyte solution containing 0.3 M 1,2-dimethyl-3-propylimidazolium iodide, 0.5 M LiI, 0.05 M I_2 and 0.5 M 4-tert-butylpyridine in acetonitrile, was sandwiched between the photoanode and the counter electrode by firm press. An adhesive tape with a thickness of approximately 50 μm was placed between the two electrodes to avoid short circuit.

2.3. Characterization of the samples

Morphological observations of the ZnO nanograss films were conducted by scanning electron microscopy (SEM, JSM-6490LV, JEOL) operated at 20 kV. Structural phase analyses were performed on a Philips X'Pert PRO X-ray diffractometer with a CuK_α radiation. The binding energy level and the binding energy of the ZnO nanograss films were measured on an X-ray photoelectron spectroscopy (XPS, Kartos Amicus, England) with a monochromatic Mg K_α radiation source at room temperature. The photovoltaic performance of the DSSC was measured by CIMPS-2 electrochemical workstation (Zahner, Germany) under simulated illumination (100 mW cm^{-2}) was provided by 150 W Xenon Arc Lamp (XBO 150 W/CR OFR, OSRAM), while the electrochemical impedance spectra (EIS) were measured at V_{OC} with a bias AC signal of 10 mV in the frequency range of 0.1–10^5 Hz under simulated illumination. The action spectra of the incident monochromatic photon to current conversion efficiency (IPCE) for the solar cells were measured over the wavelength of 430–730 nm with an IPCE measurement system (CIMPS-2, Zahner, Germany). The open circuit voltage decay (OCVD) was conducted by switching off the illumination of the solar simulator in a dark condition.

3. Results and discussion

Fig. 1 presents the SEM images of 45° tilt-view section of the ZnO nanograss films grown on FTO glasses from reaction solutions containing 0, 0.25, 0.5 and 1 mM $Al(NO_3)_3$ respectively. The morphologies revealed that hexagonal columns of ZnO crystals grew perpendicularly to the FTO substrate from all the solutions. The mean values of the ZnO nanorods including the length and the diameter were estimated from the statistical evaluations of SEM images. It can be measured that the thicknesses of ZnO nanograss films are almost *ca.* 6.5 μm, however, the mean diameters of ZnO hexagonal nanorods vary with the addition of $Al(NO_3)_3$. In comparison, the mean diameter of ZnO nanorods grown from the solution without $Al(NO_3)_3$ was about 465 nm, while those were approximately 210, 200 and 230 nm with adding 0, 0.25 and 1 mM $Al(NO_3)_3$, respectively. The results showed that the mean diameters of ZnO nanorods were significantly decreased when adding a small concentration of $Al(NO_3)_3$ in the growth solution. There was no obvious change as further increasing $Al(NO_3)_3$ concentration. That seemed the growth in *a*-direction of ZnO crystal was suppressed by Al^{3+} ions. The possible reason will be deeply discussed in the following section.

The crystallinity of the obtained samples grown on FTO substrate was investigated using X-ray diffraction analysis. The XRD patterns of the as-prepared ZnO nanograss films are

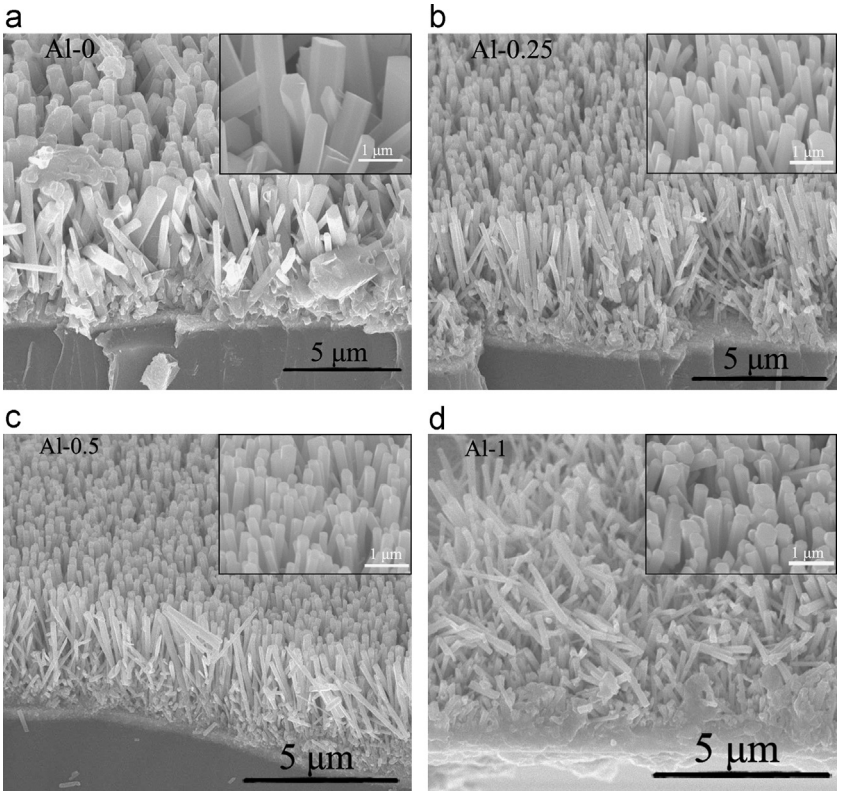

Fig. 1. FE-SEM tilt-view (45°) images of ZnO nanograss films grown under different conditions (a) 0 mM $Al(NO_3)_3$, (b) 0.25 mM $Al(NO_3)_3$, (c) 0.5 mM $Al(NO_3)_3$ and (d) 1 mM $Al(NO_3)_3$. The inserts show the high magnification images of the samples.

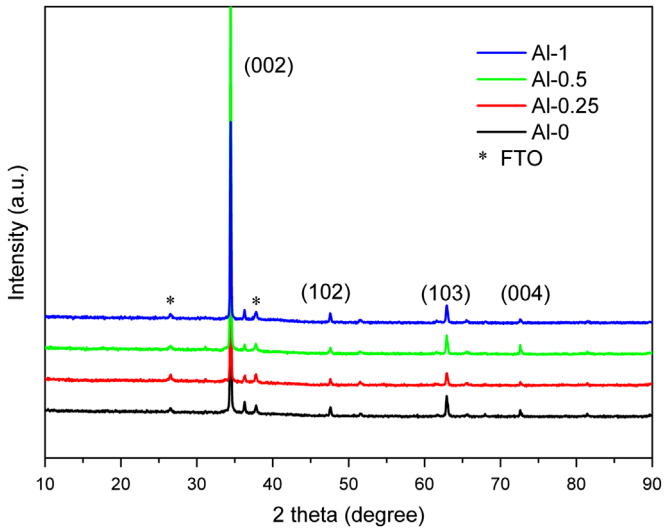

Fig. 2. X-ray diffraction patterns of ZnO nanograss films under different growth conditions on FTO glass substrates. The diffraction peaks (denoted as ∗) in all the curves are ascribed to the FTO substrate.

summarized in Fig. 2. The strongest peak located at 34.4° corresponds to the (002) crystal plane of the wurtzite ZnO. This indicates that the *c*-axis of the nanorods is perpendicular to the FTO substrate surface, which is in accordance with SEM observations as shown in Fig. 1. All diffraction peaks can be well indexed to hexagonal wurtzite ZnO (JCPDS Card No. 36-1451, $a=b=3.2498$, $c=5.2066$) except for those arising from FTO substrate (denoted as ✻). No characteristic peaks arising from reactants or intermediate products are detected, implying high purity of the prepared ZnO nanograss films.

XPS analysis was carried out to elucidate the surface chemical states and atomic compositions of the ZnO nanograss films. It was well known that the peak of Al 2p was mainly located at 74.7 eV attributed to the Al–O bonds [21]. However, no Al 2p signals were detected for all the samples of ZnO nanograss (Fig. 3). It was speculated that the aluminum atom had not been doped into ZnO lattice, but affected the growth of ZnO nanostructures by means of selective adsorptions on ZnO crystalline facets through electrostatic interaction. The O 1s peaks of the XPS spectra and their deconvolution results for ZnO nanostructures are illustrated in Fig. 3. It can be found that the typical O 1s peak of ZnO can be consistently fitted by three nearly Gaussian components, centered at 530.1 eV, 531.4 eV, and 532.5 eV, accordingly. The component on the lower binding energy side of the O 1s spectra was owing to the O^{2-} ions on wurtzite structure of hexagonal Zn^{2+} ion arrays, surrounded by Zn atoms with their full complement of nearest-neighbor O^{2-} ions [22]. The medium binding energy component, centered at 531.4 eV, was related to O^{2-} ions in oxygen defect in the skin layer of ZnO matrix, such as ZnO_x and/or Zn–OH species [23], of which the intensity could be partly linked to the variations in the concentration of oxygen vacancies. The higher peak at 532.5 eV was usually attributed to the presence of loosely bound oxygen atoms on the surface of ZnO nanograss, such as $–CO_3$, adsorbed H_2O or O_2, which could not be easily removed, even by annealing at high temperature [24]. Contrastively, the intensity percentages of

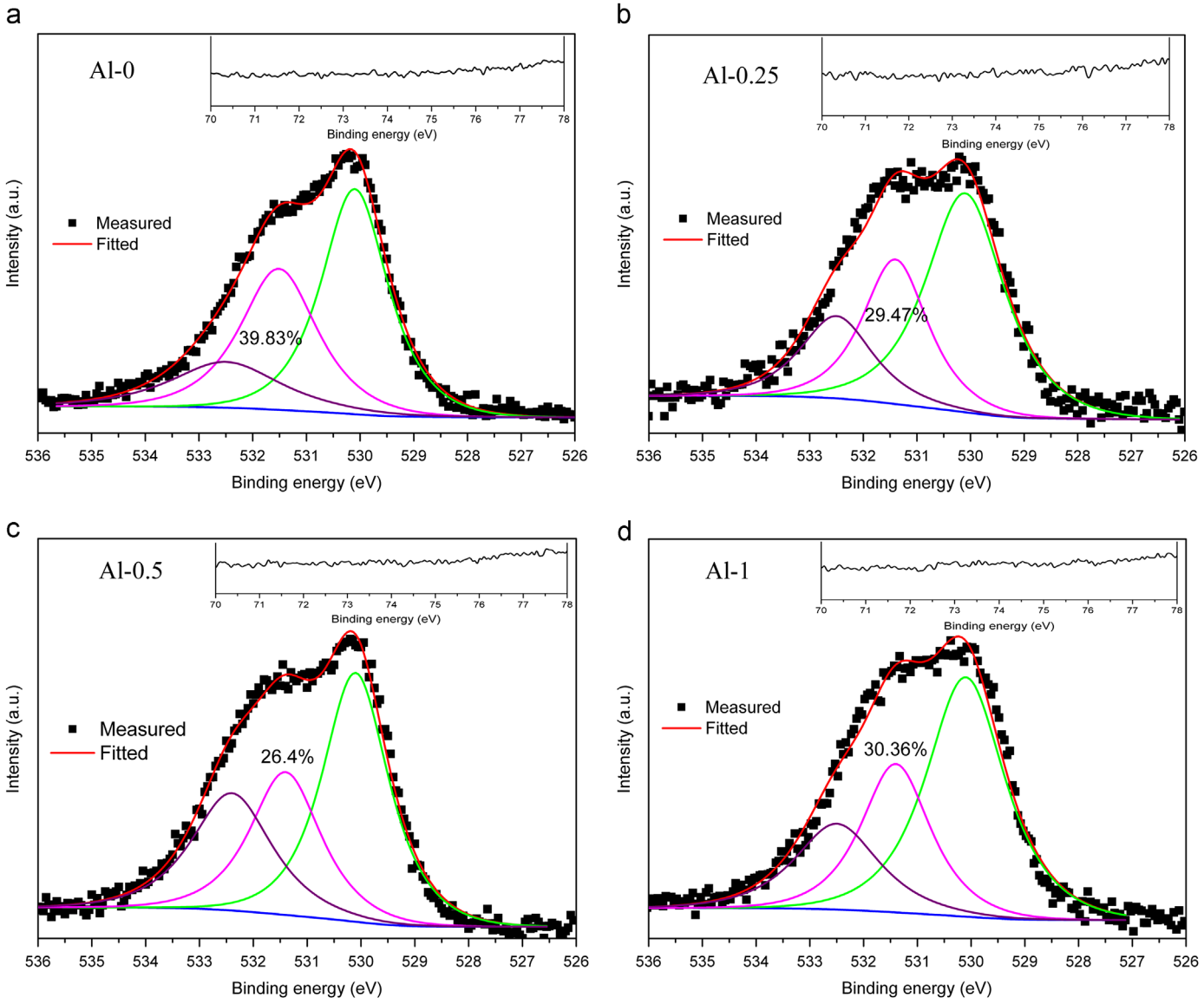

Fig. 3. High-resolution O 1s XPS spectra for the ZnO grown under different conditions (a) 0 mM $Al(NO_3)_3$, (b) 0.25 mM $Al(NO_3)_3$, (c) 0.5 mM $Al(NO_3)_3$ and (d) 1 mM $Al(NO_3)_3$. All inserts show high-resolution Al 2p XPS spectra for corresponding ZnO nanograss.

the medium binding energy components to the total O 1s peaks are 39.83%, 29.47%, 26.4% and 30.36%, respectively. It can be seen that the oxygen defect in the skin layer of ZnO decreases first with increase of Al^{3+} concentration and then increases as further increasing Al^{3+} concentration. These results indicate that the surface oxygen defect would be affected by adding Al^{3+} during the growth procedure.

The mechanism of Al^{3+} affecting ZnO nanograss growth was studied based on both morphological observations and processing hydrolyzes in the precursor solutions. In this work, HMTA was used as a weak base and pH buffer. It was generally accepted that HMTA decomposed slowly in heated aqueous solutions to yield ammonia and formaldehyde as an initial reactant, resulting in forming hydroxide ions. Then the hydroxide ions would react with Zn^{2+}, leading to continuous formation of zinc complexes, and finally convert into ZnO crystallites, growing along the *c*-axis towards ZnO nanorods. Meanwhile, as the Al^{3+} was introduced into the growth solution, some other reactions would occur. $Al(OH)_3$ would be the first compound formed in the solution, and then the successive reaction would take place between $Al(OH)_3$ and superfluous OH^-, resulting in generation of anionic AlO_2^- in the solution. The detailed chemical reactions in the whole process are given as follows [25–27]:

$$(CH_2)_6N_4+6H_2O\leftrightarrow 6HCHO+4NH_3 \quad (1)$$

$$NH_3+H_2O\leftrightarrow NH_4^+ +OH^- \quad (2)$$

$$Zn^{2+}+OH^-\leftrightarrow Zn(OH)_2\rightarrow ZnO+H_2O \quad (3)$$

$$Al^{3+}+OH^-\leftrightarrow Al(OH)_3\leftrightarrow AlO_2^- \quad (4)$$

Fig. 4 shows a schematic diagram of the proposed growth mechanisms of ZnO nanorods without or with aluminum ions. It is well known that ZnO crystal consists of oxygen

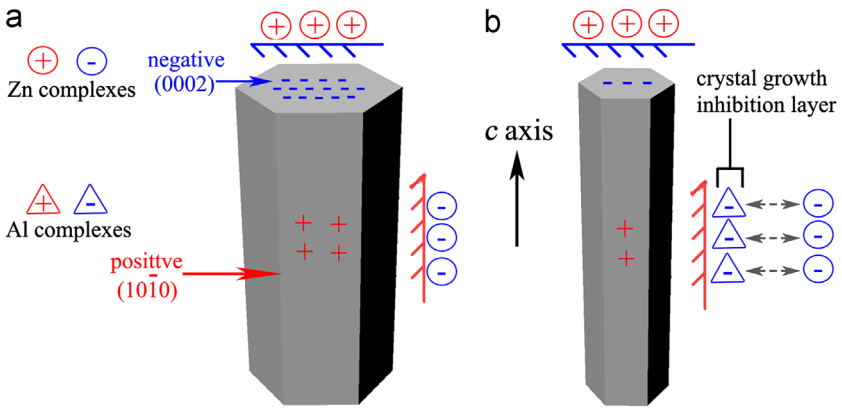

Fig. 4. Schematic diagrams for the growth of ZnO nanograss (a) without aluminum nitrate and (b) with aluminum nitrate.

and zinc atoms packing hexagonally, with top tetrahedron corner-exposed polar zinc (0001) plane, basal polar oxygen (000$\bar{1}$)plane, and six symmetric non-polar {01$\bar{1}$0} planes parallel to the [0001] direction. Generally, ZnO crystals grew preferentially along the [001] direction and form 1-D nanorods because the (0001) plane had the highest surface energy [6], as shown in Fig. 4a. From the previous research [20], it had been proven that the (0002) surface was negatively charged and {01$\bar{1}$0} surface exhibited positively charged at pH = 11. Thus, we suggested that AlO_2^- might sever as the surface-suppression agent in the reaction system, as shown in Fig. 4b. The adsorption of AlO_2^- on the {01$\bar{1}$0} surface by the electrostatic interaction formed crystal growth inhibition layer, resulting in changing the growth rate of different crystal facets. Accordingly, the intrinsic growth of ZnO along [100] direction was substantially suppressed. The passivation effects of the AlO_2^- inhibition layer resulted in increasing of the aspect ratio of ZnO nanorods, as shown in Fig. 1.

The current–voltage characteristics of ZnO nanograss based DSSC were studied under simulated sunlight with intensity of 100 mW cm^{-2}. Fig. 5 shows the measured *J–V* curves of the nanograss based DSSC fabricated with the above samples. The values of open-circuit voltage (V_{OC}), short-circuit current density (J_{SC}), fill factor (FF), and conversion efficiencies (η) of the electrodes are summarized in Table 1. All samples showed open-circuit voltage (V_{OC}) of *ca.* 0.60 V, indicating that there was no significant effect of ZnO nanorod diameter on V_{OC} of the DSSC in this study. Generally, V_{OC} of a solar cell was determined by the difference between the Fermi level for electrons in the ZnO electrode and the redox potential of I_3^-/I^- [4]. J_{SC} showed an increasing behavior first from 0.965 to 1.344 mA cm^{-2} when the aluminum ions concentration was less than 0.5 mM. Once the aluminum ions concentration exceeded 0.5 mM, J_{SC} values decreased from 1.344 to 1.155 mA cm^{-2}. Compared with the efficiency of 0.18% for the DSSC fabricated with Al-0 electrode, the optimized DSSC based on Al-0.5 photoelectrode increased the efficiency by 55.6%. Fig. 6 displays the incident photon to electron conversion efficiency (IPCE) of the DSSC as a function of the monochromatic irradiation wavelength. The maximal values of IPCE curves at the wavelength of about 525 nm were contributed to the dye absorption, resulting from the

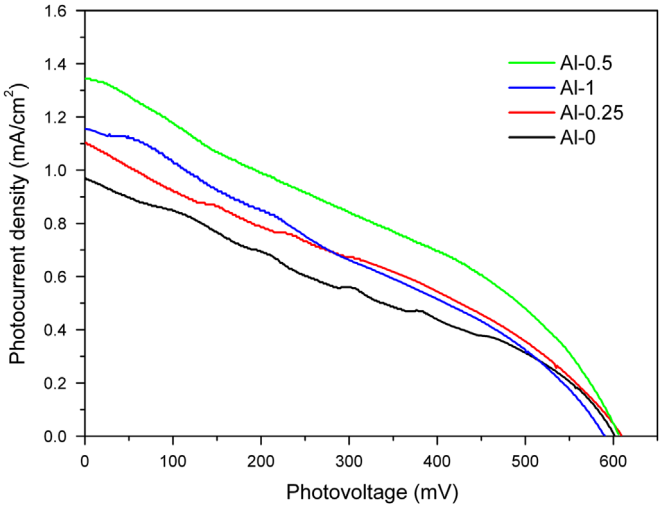

Fig. 5. Photocurrent–voltage (*J-V*) curves of DSSC fabricated with different photoelectrodes.

visible t_2–π^* metal-to-ligand charge transfer (MLCT) [28]. It could be clearly seen that the IPCE of the DSSC based on Al-0.25, Al-0.5 and Al-1 photoanodes had been improved as compared with the DSSC based on Al-0 photoanode, which agreed with the results of J_{SC}. We ascribed the majority of the improvement in cell performance to the enlargement of J_{SC} behavior in our case.

The open-circuit voltage decay (OCVD) curves can provide more information of electron recombination processes in DSSC between the ZnO electrode and electrolyte in dark [29]. Since there was no current flow through the DSSC device when the illumination of the DSSC at open circuit condition was interrupted, the excess electrons recombined with the electrolyte at the interface. Thus the photovoltage decay rate was related to electron lifetime [30]. The results of the OCVD measurements performed on the cells are reported in Fig. 7. In our case, it was evident that the decay rate of open-circuit voltage (evidencing charge lifetime) decrease first when the aluminum ions concentration was less than 0.5 mM, and then increase as the aluminum ions concentration exceeded 0.5 mM. The results indicated the highest recombination rate for Al-0 based DSSC and the slowest recombination rate for

Table 1
Cell performance of characteristics of ZnO nanograss based DSSC.

Electrode	J_{SC} (mA cm^{-2})	V_{OC} (mV)	FF	η (%)	% increase
Al-0	0.965	603	0.309	0.18	–
Al-0.25	1.102	609	0.327	0.22	22.2
Al-0.5	1.344	606	0.344	0.28	55.6
Al-1	1.155	592	0.304	0.21	16.7

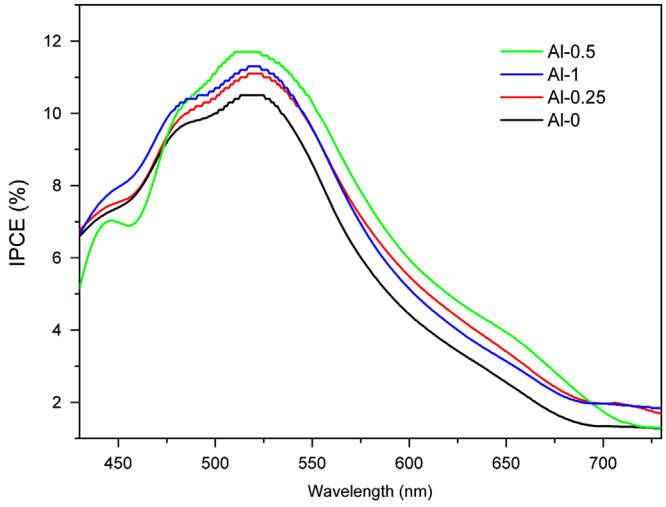

Fig. 6. The incident photo to electric conversion efficiency (IPCE) curves of the DSSC fabricated with different photoelectrodes.

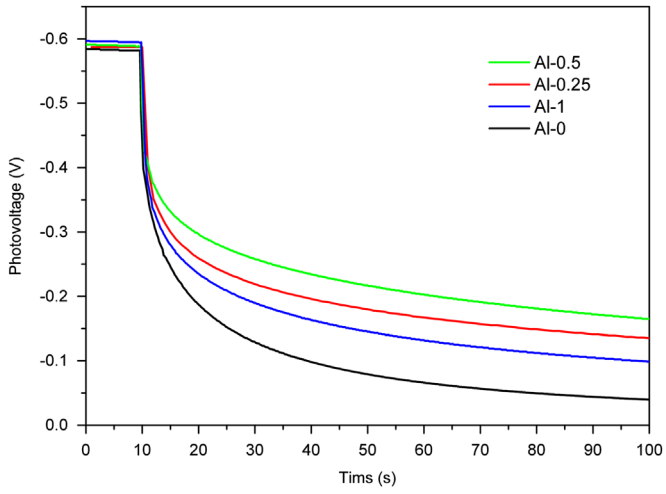

Fig. 7. Open-circuit voltage decay measurement of four DSSC fabricated with different electrodes.

Al-0.5 based DSSC. As well known, the electron lifetime was mainly affected by the surface state traps in the ZnO film. It revealed that higher electron lifetime in lower V_{OC} represented the photoanode possessed a lower surface trap density [31]. From the XPS results, it had been demonstrated that the surface oxygen defect in ZnO was affected by introducing aluminum ions, which was in well agreement with the OCVD results. On the other hand, the lower surface trap density and higher electron lifetime of Al-0.5 based photoanode were consistent with the higher FF in Al-0.5 based DSSC (as shown in Table 1).

Electrochemical impedance spectroscopy (EIS) can provide deeper understanding on the electron transfer processes in DSSC. To reveal the difference in the interfacial characteristics of these photoelectrodes, EIS was measured under the illumination (100 mW cm^{-2}) by applying a 10 mV ac signal at the bias of V_{oc} over the frequency range from 100 mHz to 100 kHz. Fig. 8 (a) and (b) shows the Nyquist and Bode plots of the ZnO nanograss DSSC, respectively. It can be seen that two well-defined semicircles are obtained in all Nyquist plots. The small semicircle in the high frequency (kHz range) fits to a charge-transfer resistance and the capacitance should be ascribed to the process at the redox electrolyte/Pt counter electrode interface. The larger semicircle in the lower frequency range (100–1 Hz) corresponds to the recombination resistance and chemical capacitance across the ZnO/dye/redox electrolyte interface, which is important in the device. The larger semicircle for Al-0.5 cell was the smallest in all samples, indicating the fastest electron/hole generation and transport as well as the lowest hole–electron recombination rate [32]. Since there was no current passing through the external circuit at V_{OC} condition, the electrons injected into the oxide semiconductor must be recombined at the metal oxide/dye/electrolyte interface. Thus, the electron lifetime in ZnO nanograss photoanodes could be calculated from the maximum angular frequency (ω_{max}) of the impedance semicircle arc at middle frequencies (1–100 Hz), according to the relation $\tau = 1/\omega_{max} = 1/2\pi f_{max}$ [33]. As shown in Fig. 8b, the characteristic frequency peak (f_{max}) values of the samples are ~23.6, ~14.2, ~12.8 and ~15.6 Hz, respectively. These observations implied that electron in Al-0.5 photoanode had a longest lifetime among the samples, which was consistent with the results of OCVD. Considering XPS, OCVD and EIS analyses, the electron lifetime of different ZnO nanograss photoanodes was mainly affected by the surface oxygen defect in ZnO, resulting in enhancement of the conversion efficiency.

4. Conclusion

In this work, ZnO nanograss films were successfully synthesized by the aqueous solution process with or without adding Al^{3+} as an additive. Detailed morphological and structural analyses indicated that the ZnO nanograss films had the hexagonal wurtzite structure perpendicular to the substrates along the [0001] direction. It was found that Al^{3+} had an obvious effect on the crystal growth of ZnO, leading to

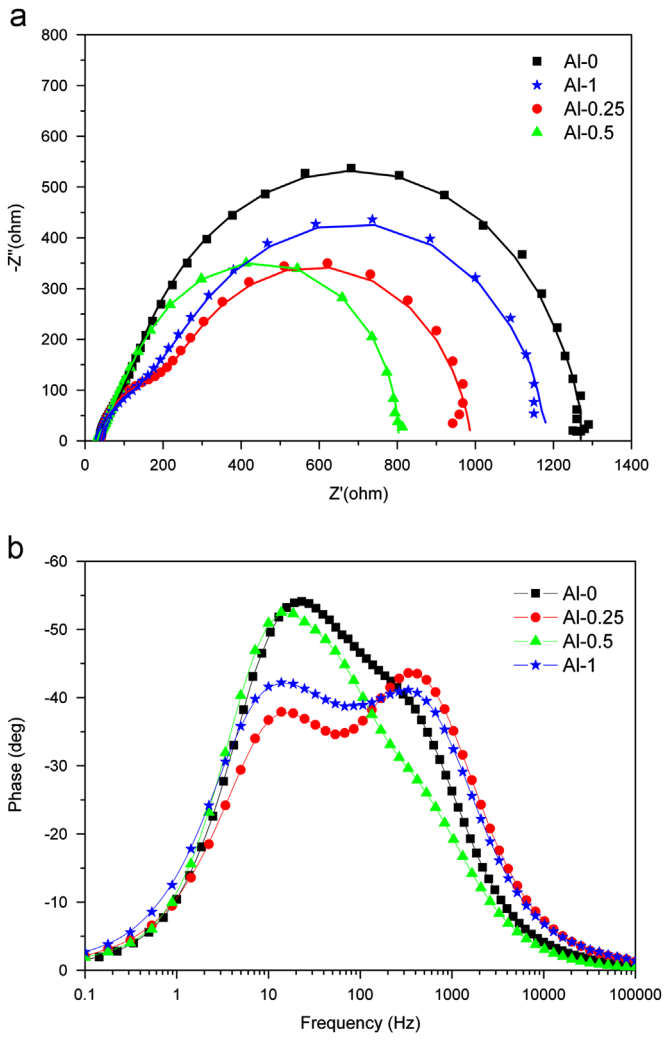

Fig. 8. Electrochemical impedance spectroscopy (EIS) of DSSC fabricated with different electrodes: (a) Nyquist plots and (b) Bode plots.

changes in morphology and aspect ratio by electrostatic interaction between ZnO crystal and Al complex. The photochemical experimental results showed that the conversion efficiency of DSSC based on Al-0.5 photoanode was increased by 55.6% compared to that of DSSC based on Al-0 photoanode. The remarkable enhancement of the photovoltaic performance was mainly attributed to the higher electron lifetime and the lower electron recombination, which was confirmed by the EIS and OCVD characterizations.

Acknowledgment

This work was financially supported by the National Natural Science Foundation of China (Nos. 51173148, 90305003), the Science and Technology Planning Project of Sichuan Province (Nos. 2010GZ0251, 2011GZX0052), and the Fundamental Research Funds for the Central Universities (Nos. SWJTU11ZT10, SWJTU11CX052). Shibu Zhu is grateful for the financial support from the Innovation Fund for Ph.D. Students of Southwest Jiaotong University.

References

[1] B. O'regan, M. Grätzel, A low-cost, high-efficiency solar cell based on dye-sensitized colloidal TiO_2 films, Nature 353 (1991) 737–740.
[2] M. Grätzel, Photoelectrochemical cells, Nature 414 (2001) 338–344.
[3] A. Yella, H.-W. Lee, H.N. Tsao, C. Yi, A.K. Chandiran, M.K. Nazeeruddin, E.W.-G. Diau, C.-Y. Yeh, S.M. Zakeeruddin, M. Grätzel, Porphyrin-sensitized solar cells with cobalt (II/III)-based redox electrolyte exceed 12 percent efficiency, Science 334 (2011) 629–634.
[4] R. Jose, V. Thavasi, S. Ramakrishna, Metal oxides for dye-sensitized solar cells, Journal of the American Ceramic Society 92 (2009) 289–301.
[5] Q. Zhang, C.S. Dandeneau, X. Zhou, G. Cao, ZnO nanostructures for dye-sensitized solar cells, Advanced Materials 21 (2009) 4087–4108.
[6] S. Xu, Z.L. Wang, One-dimensional ZnO nanostructures: solution growth and functional properties, Nano Research 4 (2011) 1013–1098.
[7] F. Xu, L. Sun, Solution-derived ZnO nanostructures for photoanodes of dye-sensitized solar cells, Energy and Environmental Science 4 (2011) 818–841.
[8] C. Kuan, M. Hon, J. Chou, I. Leu, Growth characteristics of hierarchical ZnO structures prepared by one-step aqueous chemical growth, Ceramics International 38 (2012) 1255–1260.
[9] S.B. Zhu, L.M. Shan, X.N. Chen, L. He, J.J. Chen, M. Jiang, X.L. Xie, Z.W. Zhou, Hierarchical ZnO architectures consisting of nanorod and nanosheet via a solution route for photovoltaic enhancement in dye-sensitized solar cells, RSC Advances 3 (2013) 2910–2916.
[10] M. Law, L. Greene, J. Johnson, R. Saykally, P. Yang, Nanowire dye-sensitized solar cells, Nature Materials 4 (2005) 455–459.
[11] S.H. Ko, D. Lee, H.W. Kang, K.H. Nam, J.Y. Yeo, S.J. Hong, C. P. Grigoropoulos, H.J. Sung, Nanoforest of hydrothermally grown hierarchical ZnO nanowires for a high efficiency dye-sensitized solar cell, Nano Letters 11 (2011) 666–671.
[12] Y. Shi, C. Zhu, L. Wang, W. Li, C. Cheng, K.M. Ho, K.K. Fung, N. Wang, Optimizing nanosheet-based ZnO hierarchical structure through ultrasonic-assisted precipitation for remarkable photovoltaic enhancement in quasi-solid dye-sensitized solar cells, Journal of Materials Chemistry 22 (2012) 13097–13103.
[13] Y. Lin, J. Yang, Y. Meng, Nanostructured ZnO thin films by SDS-assisted electrodeposition for dye-sensitized solar cell applications, Ceramics International 39 (2012) 5049–5052.
[14] A.B.F. Martinson, M.S. Góes, F. Fabregat-Santiago, J. Bisquert, M.J. Pellin, J.T. Hupp, Electron transport in dye-sensitized solar cells based on zno nanotubes: evidence for highly efficient charge collection and exceptionally rapid dynamics, Journal of Physical Chemistry A 113 (2009) 4015–4021.
[15] A. Martinson, J. Elam, J. Hupp, M. Pellin, ZnO nanotube based dye-sensitized solar cells, Nano Letters 7 (2007) 2183–2187.
[16] S.B. Zhu, W. Wei, X.N. Chen, M. Jiang, Z.W. Zhou, Hybrid structure of polyaniline/ZnO nanograss and its application in dye-sensitized solar cell with performance improvement, Journal of Solid State Chemistry 190 (2012) 174–179.
[17] M. McCune, W. Zhang, Y. Deng, High efficiency dye-sensitized solar cells based on three-dimensional multilayered ZnO nanowire arrays with caterpillar-like structure, Nano Letters 12 (2012) 3656–3662.
[18] S.B. Zhu, X.N. Chen, F.B. Zuo, M. Jiang, Z.W. Zhou, D. Hui, Controllable synthesis of ZnO nanograss with different morphologies and enhanced performance in dye-sensitized solar cells, Journal of Solid State Chemistry 197 (2013) 69–74.
[19] J.J. Qiu, X.M. Li, F.W. Zhuge, X.Y. Gan, X.D. Gao, W.Z. He, S.J. Park, H.K. Kim, Y.H. Hwang, Solution-derived 40 μm vertically aligned ZnO nanowire arrays as photoelectrodes in dye-sensitized solar cells, Nanotechnology 21 (2010) 195602.
[20] J. Joo, B.Y. Chow, M. Prakash, E.S. Boyden, J.M. Jacobson, Face-selective electrostatic control of hydrothermal zinc oxide nanowire synthesis, Nature Materials 10 (2011) 596–601.
[21] P.Y. Yang, J.L. Wang, W.C. Tsai, S.J. Wang, J.C. Lin, I. Lee, C. T. Chang, H.C. Cheng, Field-emission characteristics of Al-doped ZnO nanostructures hydrothermally synthesized at low temperature, Journal of Nanoscience and Nanotechnology 11 (2011) 6013–6019.

[22] S. Major, S. Kumar, M. Bhatnagar, K.L. Chopra, Effect of hydrogen plasma treatment on transparent conducting oxides, Applied Physics Letters 49 (1986) 394–396.
[23] O. Lupan, T. Pauporté, L. Chow, B. Viana, F. Pellé, L. Ono, B. Roldan Cuenya, H. Heinrich, Effects of annealing on properties of ZnO thin films prepared by electrochemical deposition in chloride medium, Applied Surface Science 256 (2010) 1895–1907.
[24] S. Yun, J. Lee, J. Yang, S. Lim, Hydrothermal synthesis of Al-doped ZnO nanorod arrays on Si substrate, Physica B 405 (2010) 413–419.
[25] B. Weintraub, Z. Zhou, Y. Li, Y. Deng, Solution synthesis of one-dimensional ZnO nanomaterials and their applications, Nanoscale 2 (2010) 1573–1587.
[26] Y. Lee, Y. Zhang, S.L.G. Ng, F.C. Kartawidjaja, J. Wang, Hydrothermal growth of vertical ZnO nanorods, Journal of the American Ceramic Society 92 (2009) 1940–1945.
[27] J. Liu, L. Xu, B. Wei, W. Lv, H. Gao, X. Zhang, One-step hydrothermal synthesis and optical properties of aluminium doped ZnO hexagonal nanoplates on a zinc substrate, CrystEngComm 13 (2011) 1283–1286.
[28] H.-M. Cheng, W.-H. Chiu, C.-H. Lee, S.-Y. Tsai, W.-F. Hsieh, Formation of branched ZnO nanowires from solvothermal method and dye-sensitized solar cells applications, Journal of Physical Chemistry C 112 (2008) 16359–16364.
[29] J. Bisquert, A. Zaban, M. Greenshtein, I. Mora-Seró, Determination of rate constants for charge transfer and the distribution of semiconductor and electrolyte electronic energy levels in dye-sensitized solar cells by open-circuit photovoltage decay method, Journal of the American Chemical Society 126 (2004) 13550–13559.
[30] A. Zaban, M. Greenshtein, J. Bisquert, Determination of the electron lifetime in nanocrystalline dye solar cells by open-circuit voltage decay measurements, ChemPhysChem 4 (2003) 859–864.
[31] F. Fabregat-Santiago, J. García-Cañadas, E. Palomares, J.N. Clifford, S. A. Haque, J.R. Durrant, G. Garcia-Belmonte, J. Bisquert, The origin of slow electron recombination processes in dye-sensitized solar cells with alumina barrier coatings, Journal of Applied Physics 96 (2004) 6903–6907.
[32] Z. Li, Y. Zhou, G. Xue, T. Yu, J. Liu, Z. Zou, Fabrication of hierarchically assembled microspheres consisting of nanoporous ZnO nanosheets for high-efficiency dye-sensitized solar cells, Journal of Materials Chemistry 22 (2012) 14341–14345.
[33] R. Kern, R. Sastrawan, J. Ferber, R. Stangl, J. Luther, Modeling and interpretation of electrical impedance spectra of dye solar cells operated under open-circuit conditions, Electrochimica Acta 47 (2002) 4213–4225.